

Structure, Bonding, and Catalytic Activity of Monodisperse, Transition-Metal-Substituted CeO₂ Nanoparticles

Joseph S. Elias,^{*,†} Marcel Risch,[‡] Livia Giordano,^{⊥,||} Azzam N. Mansour,[#] and Yang Shao-Horn^{*,‡,§,||}

[†]Department of Chemistry, [‡]Research Laboratory of Electronics, [§]Department of Materials Science and Engineering, and

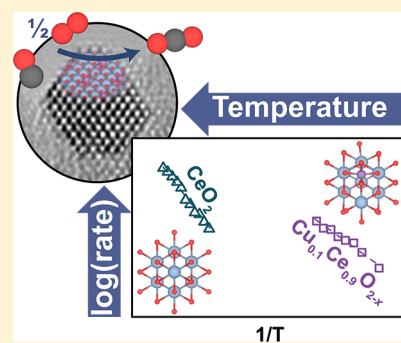
^{||}Department of Mechanical Engineering, Massachusetts Institute of Technology, Cambridge, Massachusetts 02139, United States

[⊥]Dipartimento di Scienza dei Materiali, Università di Milano-Bicocca, Via R. Cozzi 53, 20125 Milano, Italy

[#]Naval Surface Warfare Center, Carderock Division, 9500 MacArthur Boulevard, West Bethesda, Maryland 20817-5700, United States

Supporting Information

ABSTRACT: We present a simple and generalizable synthetic route toward phase-pure, monodisperse transition-metal-substituted ceria nanoparticles ($M_{0.1}Ce_{0.9}O_{2-x}$, $M = Mn, Fe, Co, Ni, Cu$). The solution-based pyrolysis of a series of heterobimetallic Schiff base complexes ensures a rigorous control of the size, morphology and composition of 3 nm $M_{0.1}Ce_{0.9}O_{2-x}$ crystallites for CO oxidation catalysis and other applications. X-ray absorption spectroscopy confirms the dispersion of aliovalent (M^{3+} and M^{2+}) transition metal ions into the ceria matrix without the formation of any bulk transition metal oxide phases, while steady-state CO oxidation catalysis reveals an order of magnitude increase in catalytic activity with copper substitution. Density functional calculations of model slabs of these compounds confirm the stabilization of M^{3+} and M^{2+} in the lattice of CeO₂. These results highlight the role of the host CeO₂ lattice in stabilizing high oxidation states of aliovalent transition metal dopants that ordinarily would be intractable, such as Cu³⁺, as well as demonstrating a rational approach to catalyst design. The current work demonstrates, for the first time, a generalizable approach for the preparation of transition-metal-substituted CeO₂ for a broad range of transition metals with unparalleled synthetic control and illustrates that Cu³⁺ is implicated in the mechanism for CO oxidation on CuO-CeO₂ catalysts.



INTRODUCTION

Because of the interesting physical and chemical properties of cerium(IV) oxide (CeO₂, ceria), including reversible surface oxygen ion exchange^{1,2} and electronic/ionic conductivity,³ ceria-based materials have been studied for a number of applications including the oxidation of carbon monoxide (CO) and hydrocarbon-based fuels,⁴ the water–gas shift reaction,⁵ photoinduced water splitting,⁶ oxygen-conducting membranes for solid-oxide fuel cells,⁷ flue-gas desulfurization reactions,⁸ the production of hydrogen by the steam reforming of methanol,⁹ and sensor applications.¹⁰ Introduction of redox active cations, especially of aliovalent transition metals, into the lattice of CeO₂ to form the solid solution $M_yCe_{1-y}O_{2-x}$ imparts added functionality to this class of materials. The dramatic increase in activity for the water–gas shift reaction with incorporation of nonmetallic Au and Pt species into the lattice of CeO₂ is a notable example,⁵ while applications of substitution into CeO₂ outside of heterogeneous catalysis include band gap engineering in photovoltaic devices.¹¹ Unfortunately, traditional methods for the preparation of aliovalent substituted CeO₂, especially with transition metal substitution, often leads to the formation of multiple phases, polydisperse crystallite sizes and disparate crystallite habits. The presence of impurity phases along with differences in crystallite size and surface termination all influence the kinetics of CO oxidation on $M_yCe_{1-y}O_{2-x}$ catalysts. To establish the influence of transition metal

substitution in CeO₂ on the kinetics of CO oxidation necessitates the preparation of a library of these catalysts with superior homogeneity in phase, crystallite size and crystallographic termination. The presence of inseparable impurities complicates even the identification of the oxidation state and local structure of M in $M_yCe_{1-y}O_{2-x}$. Taking a notable example from heterogeneous catalysis, traditional methods for the preparation of the solid solution $Cu_yCe_{1-y}O_{2-x}$, including coprecipitation^{4,12–15} and excess-solution impregnation^{16–18} techniques, lead to the formation of the solid solution in addition to dispersed CuO phases in these so-called CuO-CeO₂ catalysts, which prevents the rigorous identification of the catalytic site for CO oxidation.^{19,20}

Here we report a generalizable synthetic strategy for the preparation of monodisperse, phase-pure nanocrystals of $M_{0.1}Ce_{0.9}O_{2-x}$ with aliovalent transition metal substitution ($M = Mn, Fe, Co, Ni$ and Cu). X-ray absorption spectroscopy at the transition metal L-, K-, cerium L- and oxygen K-edges confirms that the transition metal species are stabilized in the 3+ oxidation state upon incorporation into the CeO₂ lattice, in contrast to previous studies on CuO-CeO₂.^{4,15} CO oxidation on $Cu_{0.1}Ce_{0.9}O_{2-x}$ reveals that Cu species in the lattice are responsible for an increase in catalytic activity by an order of

Received: September 6, 2014

magnitude in comparison to undoped, nanocrystalline CeO₂. This finding provides insights into developing novel strategies to design highly active and uniform catalysts for the oxidation of CO and hydrocarbon fuels and for other applications.

RESULTS AND DISCUSSION

Synthesis of M_{0.1}Ce_{0.9}O_{2-x}. Monodisperse, hexanesoluble single crystallites of oleylamine-stabilized M_{0.1}Ce_{0.9}O_{2-x} (M = Mn, Fe, Co, Ni, Cu) were prepared according to Figure 1. The synthetic scheme involves the

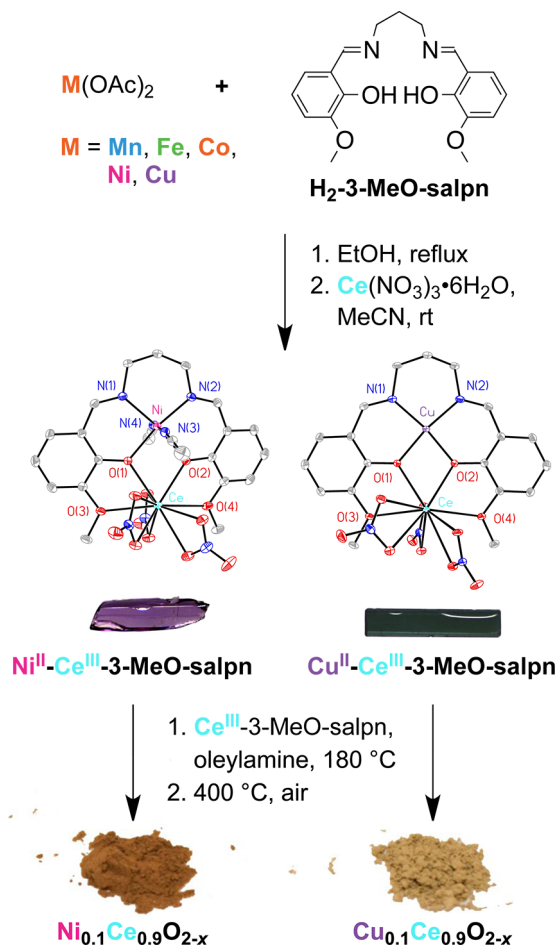


Figure 1. Synthesis of M_{0.1}Ce_{0.9}O_{2-x} from heterobimetallic 3-MeO-salpn complexes. Representative crystal structures for Ni^{II}-Ce^{III}-3-MeO-salpn and Cu^{II}-Ce^{III}-3-MeO-salpn are included, with thermal ellipsoids plotted at 50% probability and hydrogen atoms omitted for clarity.

preparation and subsequent decomposition of a library of heterobimetallic Schiff base complexes^{21–24} derived from the ligand *N,N'*-bis(3-methoxysalicylidene)-propylene-1,3-diamine (H₂-3-MeO-salpn). After the initial coordination of the transition metal into the inner N₂O₂ site of H₂-3-MeO-salpn, the outer O₄ lacunary site is poised for coordination of hard Lewis-acidic rare earth ions, such as Ce³⁺ (Figure 1). The choice of heterobimetallic Schiff base complexes as inorganic precursors was made in order to ensure close association between cerium and transition metal ions during the nucleation and growth of the M_{0.1}Ce_{0.9}O_{2-x} crystallites in solution, thereby preventing the formation of separate bulk transition metal oxide phases.

Single crystals of M-Ce^{III}-3-MeO-salpn (M = Co^{III}, Ni^{II}, Cu^{II}) suitable for X-ray crystal structure analysis were obtained from the slow evaporation of the complexes in acetonitrile solutions. The crystal structures of the novel M-Ce^{III}-3-MeO-salpn complexes were found to share similar structural motifs (Figures 1 and S1, Supporting Information). Coordination around the transition metal site is square planar with respect to the N₂O₂ pocket of the 3-MeO-salpn ligand. 6-Fold coordination to the nickel center of Ni^{II}-Ce^{III}-3-MeO-salpn is completed by two axially coordinated acetonitrile molecules (Figure 1) while the 6-fold coordination of the cobalt center of Co^{III}-Ce^{III}-3-MeO-salpn is achieved by two acetate groups that bridge with the cerium center (Figure S1). The copper center is 5-coordinate with a long (2.4236 Å) axial Cu–O bond to a nitrate group that bridges the two asymmetric units that make up the unit cell of Cu^{II}-Ce^{III}-3-MeO-salpn (Figure S2). Trivalent cerium ions were shown to occupy the lacunary O₄ site, bridging the transition metal via a pair of μ²-phenoxy groups, resulting in short M–Ce interatomic distances (3.3613, 3.5617, and 3.5848 Å for the cobalt, nickel and copper crystal structures, respectively). FTIR (Figure S3), ¹H NMR (Figures S4–S10) and elemental analysis (see Experimental Methods in the Supporting Information) confirm the formulas we report here for Mn^{II}-Ce^{III}-3-MeO-salpn, Fe^{III}-Ce^{III}-3-MeO-salpn and Ce^{III}-3-MeO-salpn.

With a library of homologous heterobimetallic precursors in hand, monodisperse M_{0.1}Ce_{0.9}O_{2-x} and CeO₂ nanoparticles were prepared through the pyrolysis of the precursors in oleylamine solutions under an argon atmosphere (Figure 1). Powder X-ray diffraction (PXRD) patterns for as-synthesized M_{0.1}Ce_{0.9}O_{2-x} (Figure 2) indicate a single crystalline phase,

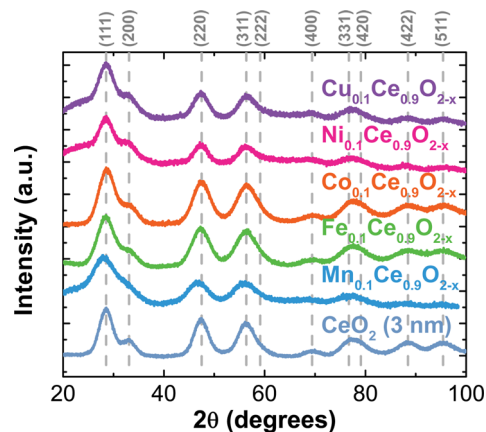


Figure 2. PXRD patterns for as-synthesized nanocrystalline M_{0.1}Ce_{0.9}O_{2-x} and CeO₂ compounds taken at room temperature (copper Kα source).

attributed to the fluorite structure of CeO₂ (space group #225, *Fm* $\bar{3}$ *m*). Scherrer analysis of peak broadening shows average crystallite sizes of 2–3 nm for M_{0.1}Ce_{0.9}O_{2-x} and CeO₂ (Figures S11–12A,C,E and Table S2). Profile fitting of PXRD data revealed that CeO₂ nanoparticles have a lattice parameter *a* (5.42 Å) that is slightly larger than that of bulk CeO₂ (5 μm) found in this study and in previous work (5.41 Å),²⁵ which can be attributed to the presence of Ce³⁺ and oxygen vacancies on the particle surface.^{26,27} The lattice expansion found for 3 nm CeO₂ is not as drastic as reported earlier for similarly sized ceria nanoparticles (5.4343²⁸ and 5.5420 Å²⁵). The disparate synthesis and annealing conditions

reported elsewhere^{25,28} may give rise to different amounts of oxygen vacancies in ceria, and help explain such a discrepancy in reported lattice parameter values in nanoparticulate CeO₂. Similarly, the lattice parameters found for M_{0.1}Ce_{0.9}O_{2-x} nanoparticles (Table S2) were also larger than that found for 5 μm CeO₂. HRTEM particle-size analysis (Figure 3) confirms

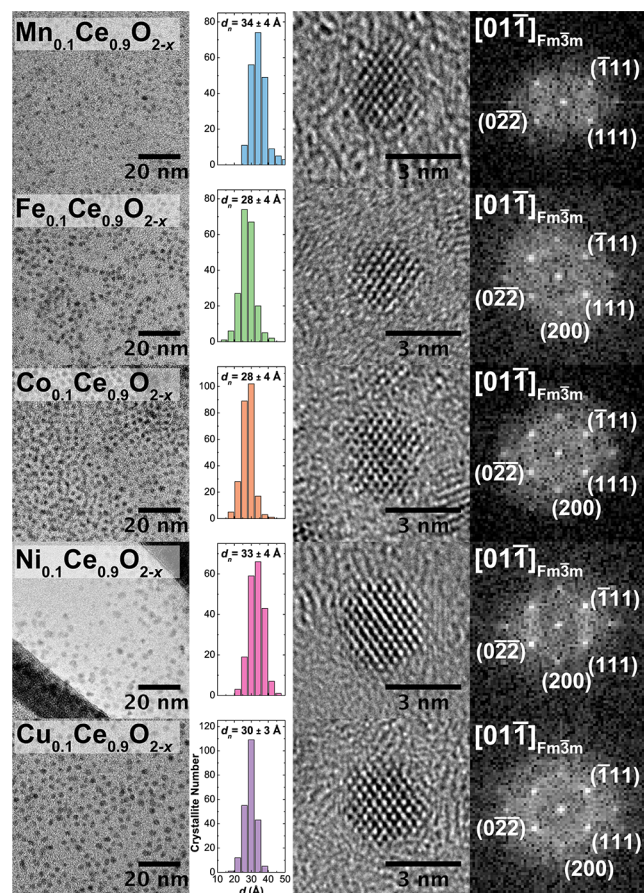


Figure 3. TEM, histogram of particle sizes, HRTEM and FFT images of as-synthesized M_{0.1}Ce_{0.9}O_{2-x}.

a narrow size distribution of 3.0 (±0.4) nm crystallites for M_{0.1}Ce_{0.9}O_{2-x}. Closer inspection by HRTEM (Figure 3, right panels) suggests that the individual crystallites exhibit a truncated octahedral crystal habit, with crystal planes terminated in eight {111} hexagonal facets and four {100} square facets (Figure S13B,C,D), a common crystallite shape reported for ceria nanoparticles.²⁹

Before further characterization, the M_{0.1}Ce_{0.9}O_{2-x} samples were annealed in air at 400 °C to remove the capping oleylamine layer, as revealed by thermogravimetric analysis (TGA, Figure S14). Preliminary ambient pressure XPS measurements of M_{0.1}Ce_{0.9}O_{2-x} at 400 °C in 75 mTorr O₂ suggests that all carbon is removed from the surface of these catalysts after annealing. PXRD (Figures S11–12B,D,F and S15 and Table S2) and HRTEM (Figure S16) suggest that during the annealing treatment, the mean size of the crystallites increases by as much as 1 nm, presumably through an Ostwald ripening or oriented agglomeration process.³⁰ Energy dispersive X-ray spectroscopy (EDS) confirms that the average transition metal substitution is between 8 and 14 mol % (Figure S17 and Table S2), which is verified by inductively coupled plasma atomic emission spectroscopy (ICP-AES, Table S2). Percent

substitution as determined by EDS with a typical experimental uncertainty of 10% in the measured values is in reasonable agreement with the values determined by ICP-AES. Since making Cu_yCe_{1-y}O_{2-x} with percent substitution *y* greater than 10% leads to the formation of multiple phases, we set the limit of substitution for all transition metal samples to *y* ≈ 10%.

Identification of the Local Structure of Transition Metal Ions in M_{0.1}Ce_{0.9}O_{2-x}. In order to identify the local atomic structure of these catalysts, especially of the redox-active transition metal centers, we turned our attention to X-ray absorption spectroscopy (XAS). The general features of the Ce L_{III}-edge spectra (Figures 4A,B and S18–20A,B and Tables S4 and S5) are similar to that of nanocrystalline CeO₂, indicating that the local coordination and oxidation-state of cerium is maintained in M_{0.1}Ce_{0.9}O_{2-x}. In the XANES region (Figure 4A and S18–20A) the intensity of the white line at 5729.6 eV decreases for all M_{0.1}Ce_{0.9}O_{2-x} and 3 nm CeO₂ compared to bulk (5 μm) CeO₂, which can be attributed to the decrease in covalency between Ce(4*f*) and O(2*p*) found as the particle size of CeO₂ decreases.³¹ Importantly, the intensity of the shoulder at 5724.5 eV, which is attributed to surface Ce³⁺,³¹ does not change with transition metal substitution. Also noteworthy is that the magnitude of the scattering path (*R* = 2.3 Å) corresponding to the first coordination shell in the EXAFS (Figures 4B, S18–S20B and Tables S4 and S5, representing eight-coordinate cerium in CeO₂) is lower for M_{0.1}Ce_{0.9}O_{2-x} and CeO₂ nanoparticles than for bulk (5 μm) CeO₂. Along with this, we found that the magnitudes of the next-nearest neighbor scattering paths (Ce–Ce and Ce–O distances, respectively, *R* = 3.9 and 4.6 Å) also decrease slightly with transition metal substitution (Figures 4B, S18–S20B and Table S4). These results, which we also found for 3 nm CeO₂ nanoparticles, support the formation of higher concentrations of undercoordinated surface CeO₂ sites with decreasing particle size, which is in good agreement with previous work on CeO₂ nanoparticles.³¹ It should be noted here, as a caveat, that the analysis of the EXAFS of Ce L_{III} spectra of materials based on CeO₂ is rather tenuous.³¹ The fact that the spectra exhibit two white lines suggests, as has previously been discussed at length,^{32,33} a many-body electronic ground state in CeO₂ (i.e., one which exhibits substantial configuration interaction between multiple electronic configurations). Therefore, the one-electron theory often used in EXAFS simulations³⁴ does not apply to such oxides. Furthermore, since both the mean squared displacement (σ^2) and scattering path degeneracy (*N*) contribute to the magnitude of the EXAFS, a rigorous determination of coordination number could not be accomplished without temperature-dependent studies. The lower intensity magnitudes in the EXAFS are likely due to a combination of smaller values for *N* (as in Table S4) and larger values for σ^2 (as in Table S5), both of which are consistent with aliovalent substitution into the CeO₂ lattice.

This comparison of the Ce L_{III}-edge XAS spectra confirms that the local geometric and electronic structure of Ce in M_{0.1}Ce_{0.9}O_{2-x} remains unaltered compared to CeO₂ nanoparticles. This assertion is further supported by spectra at the oxygen K-edge (Figure 5A). Spectra for Cu_{0.1}Ce_{0.9}O_{2-x} are identical to unsubstituted 3 nm CeO₂, exhibiting peaks at 533.7 eV without features at lower energies, which reflects that the local density of states around the oxygen ligands is predominantly unperturbed compared to CeO₂. In contrast, the O K-edge spectra for YBa₂Cu₃O_{7-δ} (YBCO) and KCuO₂ exhibit peaks at 532 eV. The peaks at 532 eV are assigned to

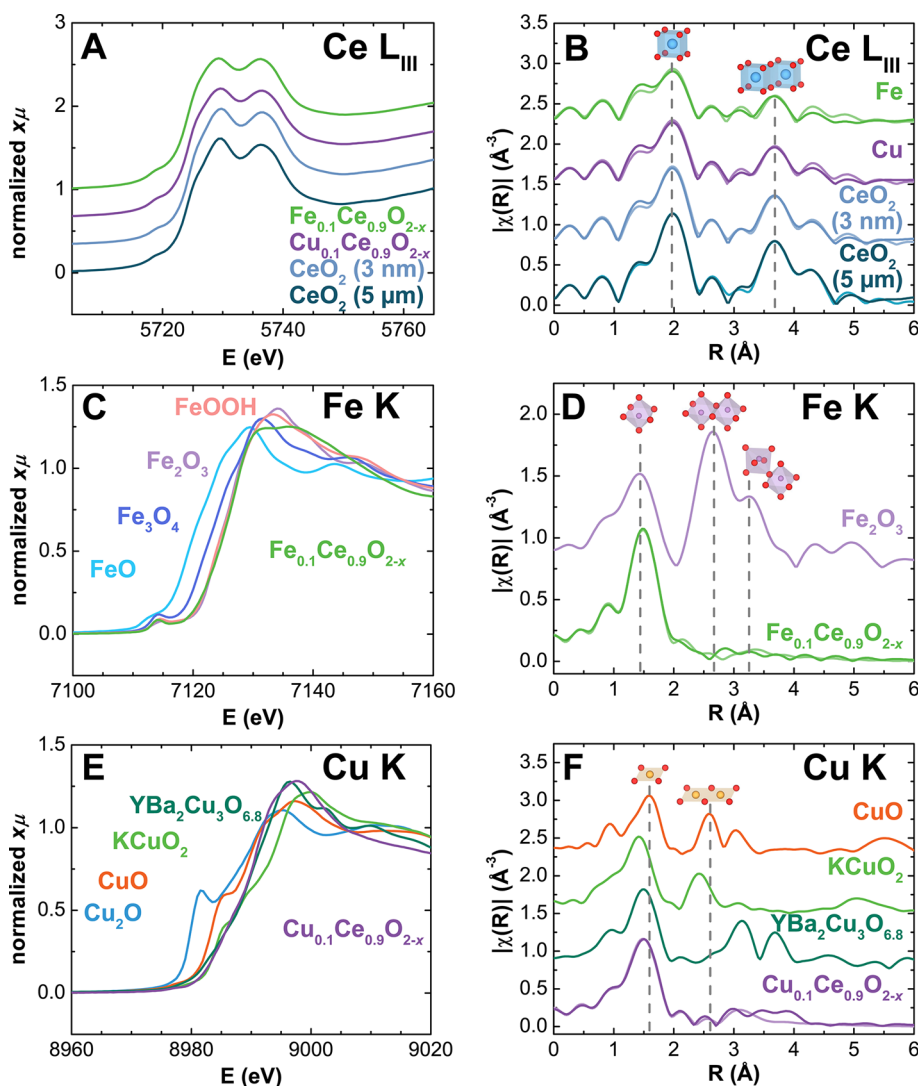


Figure 4. Cerium L_{III}-edge and transition metal K-edge XAS spectra for annealed CeO₂, Cu_{0.1}Ce_{0.9}O_{2-x} and Fe_{0.1}Ce_{0.9}O_{2-x} samples. (A) Cerium L_{III}-edge XANES spectra and (B) the magnitude of the k^2 -weighted Fourier transform of the EXAFS of Cu_{0.1}Ce_{0.9}O_{2-x} (purple), Fe_{0.1}Ce_{0.9}O_{2-x} (green) and ceria references. (C) Iron K-edge XANES spectra and (D) the magnitude of the k^2 -weighted Fourier transform of the EXAFS of Fe_{0.1}Ce_{0.9}O_{2-x} (green) and relevant iron oxides. (E) Copper K-edge XANES spectra and (F) the magnitude of the k^2 -weighted Fourier transform of the EXAFS of Cu_{0.1}Ce_{0.9}O_{2-x} (purple) and relevant copper oxides. Ce L_{III}-edge spectra were collected in transmission mode, while Cu and Fe K-edge spectra were collected in total fluorescence yield mode. Lighter traces in (B), (D) and (F) are results of EXAFS fitting (see Tables S5 and S6).

transitions into holes in the $2p$ band of oxygen, an indication of charge-transfer in formally trivalent copper compounds.^{35,36} Any contributions from oxygen ligands associated with Cu ions to the XAS spectrum either share features with the spectra of CuO or CeO₂ or are too low in intensity to be distinguished from the spectrum of CeO₂.

The transition metal K-edge XAFS spectra for M_{0.1}Ce_{0.9}O_{2-x} are presented in Figures 4C–F and S18–20C,D. Analysis of the edge-shift in the XANES region (Figure S21) suggests the presence of formally trivalent transition metal substitution. In addition, EXAFS fitting (Figures 4D,F and S19–20D and Table S6) indicates that the transition metal ions incorporate into the lattice of CeO₂ either as isolated ions or as small oxide clusters rather than form extended MO_x phases. Using the binary transition metal oxides (Fe₂O₃, Co₃O₄ and NiO) as starting models for EXAFS fitting (Table S6), we found that oxygen coordination around the transition metal was significantly smaller (~ 4) than expected for the binary oxides (6). Additionally, the number of nearest neighbor transition metal

centers was found to be much smaller (<1) than expected for extended crystalline MO_x phases. It should be noted that the model did not fit the low-magnitude data well after apparent distances longer than 3 Å, which suggests a spatial averaging of several different secondary coordination sphere configurations in the CeO₂ host lattice. These data show that our synthetic approach is generalizable; a comparison of the intrinsic properties as a function of transition metal substitution is meaningful as the M_{0.1}Ce_{0.9}O_{2-x} powders are free from any “bulk” transition-metal-oxide impurity phases.

The Cu K-edge XAS spectra of Cu_{0.1}Ce_{0.9}O_{2-x} show some surprising features in Figure 4E,F. The edge position for Cu_{0.1}Ce_{0.9}O_{2-x} is a full 3.2 eV higher than that of CuO, which indicates a formal valence higher than 2+ (a mixture of 2+ and 3+, Figure 4E). Indeed, the edge energy (taken as the energy at half step-height) corresponds to a formal oxidation state of 2.9+ when fit to a calibration curve of the edge energies of copper oxide references (Figure S21). The weak pre-edge feature at 8977 eV corroborates the presence of Cu³⁺; this feature

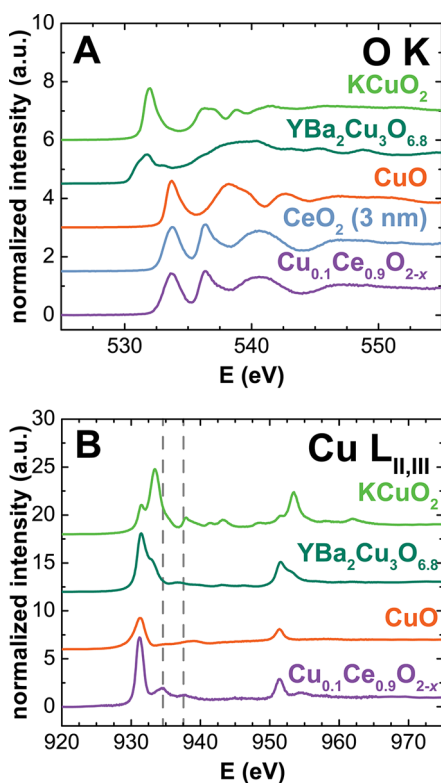


Figure 5. Oxygen K-edge and copper L_{II,III}-edge XAS spectra, collected in partial fluorescence yield mode, for annealed Cu_{0.1}Ce_{0.9}O_{2-x}. (A) Oxygen K-edge XAS spectra and (B) copper L_{II,III}-edge XAS spectra of Cu_{0.1}Ce_{0.9}O_{2-x} (purple) and reference oxides. Dashed gray lines represent charge-transfer multiplet satellites for Cu³⁺.

corresponds to the quadrupole-allowed $1s \rightarrow 3d$ transition, necessitating an unfilled $3d$ manifold for Cu.³⁷ It should be noted here that the calculated valence of +2.9 should be taken as an upper bound, as transition metal K-edge XAS mainly probes the dipole-allowed $1s \rightarrow 4p$ transition and hence does not give direct information about the unfilled $3d$ states of copper. A more suitable method would be transition metal L-edge XAS (*vide infra*), which probes the $2p \rightarrow 3d$ transition.

Fitting the EXAFS to a cluster model of CuO (Figure 4F and Table S6), the dominant Cu–O bond distance was found to be 1.93 Å, which is intermediate to the values for KCuO₂ (1.85 Å fit here and 1.83 Å from neutron diffraction studies³⁸) and CuO (1.95 Å), which suggests a 20% contribution of Cu³⁺ to the EXAFS of Cu_{0.1}Ce_{0.9}O_{2-x}. Additionally, the magnitudes of the next-nearest neighbor Cu–Cu peaks (indicating edge and corner sharing square-planar CuO₄ motifs) are greatly reduced in Cu_{0.1}Ce_{0.9}O_{2-x} (0.6) compared to crystalline CuO (8) as was the case for the other transition metals. This observation suggests the incorporation of Cu ions into the lattice of CeO₂ and not the formation of a separate, amorphous CuO phase as discussed previously.¹² Our DFT + *U* calculations show that phase separation of bulk Cu_{0.1}Ce_{0.9}O_{2-x} into stoichiometric CeO₂ and CuO is exothermic by 2.4 electron volts (Table S7), suggesting that our synthetic route affords the formation of a metastable solid-solution phase. These computed energies do not take configurational entropy into account, which necessitates further computational work on the exergonicity of phase separation in these materials.

The presence of Cu³⁺ in Cu_{0.1}Ce_{0.9}O_{2-x} is further supported by soft X-ray absorption at the Cu L-edge. Cu L_{II,III}-edge XAS

data (probing the transition $2p \rightarrow 3d$) can provide information on the density of states of the copper $3d$ band. The Cu L_{II,III}-edge XAS spectra for Cu_{0.1}Ce_{0.9}O_{2-x} and reference compounds (CeO₂, CuO, YBCO and KCuO₂), collected in the partial fluorescence yield (PFY) mode, are given in Figure 5B. The prominent local maximum at 931 eV for Cu_{0.1}Ce_{0.9}O_{2-x} has been assigned to the $2p^63d^9 \rightarrow 2p^53d^{10}$ transition,^{39–41} indicative of divalent copper centers as can be found in CuO, YBCO and (as a minor impurity) in KCuO₂. The satellite structures found at 934.5 and 937.5 eV in the XAS spectrum of Cu_{0.1}Ce_{0.9}O_{2-x} indicate the presence of Cu³⁺, as these features are similar to those of the trivalent compound KCu(biuret)₂⁴² and other formally trivalent copper compounds.^{40,41} These features are significantly lower in energy to be attributed to transitions to the final state $2p^53d^94s^1$ of CuO (~938.7 eV)³⁵ and are too high in energy to be attributed to Cu⁺ impurities (933.7 eV for Cu₂O).³⁹

Although further studies are required, including a rigorous treatment of charge-transfer multiplet theory, suffice to say that copper sites in Cu_{0.1}Ce_{0.9}O_{2-x} exist as an admixture of Cu²⁺ and Cu³⁺. Thus, we have demonstrated the preparation of a rare example of an air-stable Cu³⁺-containing oxide. Typically, the ternary and quaternary Cu³⁺ oxides, such as KCuO₂ and YBCO, are unstable in air.⁴³ For example, NaCuO₂ and KCuO₂ readily decompose in the presence of moisture to CuO with concurrent evolution of O₂. The CeO₂ lattice seems to play an important role in stabilizing copper in the trivalent state. Previous DFT studies have also highlighted the role of electropositive elements (in our case, Ce⁴⁺) in stabilizing Cu³⁺ in oxides.⁴⁴ This hypothesis is further supported by our own DFT + *U* calculations.

Our DFT + *U* calculations show that, under our annealing conditions, Cu exists as a mixture of Cu³⁺ and Cu²⁺ (Figure 6A), consistent with our XAS results. At 700 K under 21% O₂, the Gibbs energy of formation (ΔG_F , see Experimental Methods in the Supporting Information) for the Cu³⁺₂Ce₃₄O₇₁ and Cu²⁺₂Ce₃₄O₇₀ slab models are nearly identical, suggesting not only that copper exists as a mixture of Cu³⁺ and Cu²⁺, but also that the Cu^{3+/2+} couple is accessible in these materials, which may have important implications for catalysis. Understanding the physical origin for the stabilization of Cu³⁺ warrants further study, but presumably it results from a thermodynamic compromise between the copper species favoring oxidation states lower than the isoivalent case (Cu⁴⁺) and the disruption of the CeO₂ lattice by removal of charge-compensating oxygen atoms for aliovalent (Cu³⁺ and Cu²⁺) substitution. The optimized geometry of the Cu³⁺₂Ce₃₄O₇₁ model (Figure 6C) is also consistent with our EXAFS results. We found that copper is substituted into the CeO₂ lattice as square planar CuO₄ moieties that lie flat along the (100) lattice plane and relax along [100] toward the (100) plane of oxygen atoms to compensate for a shorter Cu–O bond compared to that of CeO₂ (Figure 6B,C).

An important parameter to determine for oxide materials, especially in the realm of heterogeneous catalysis, is the oxygen nonstoichiometry (x in M_{0.1}Ce_{0.9}O_{2-x}), which is related to the oxygen-ion vacancy content of these materials. The oxygen-ion vacancy contents for the M_{0.1}Ce_{0.9}O_{2-x} compounds were determined by TGA analysis and X-ray photoelectron spectroscopy (XPS) at the Ce $3d$ region. The results of these measurements (Figures S22 and S23 and Table S8 of the Supporting Information) suggest that the content of oxygen-ion vacancies in nanoparticulate ceria is relatively unchanged with

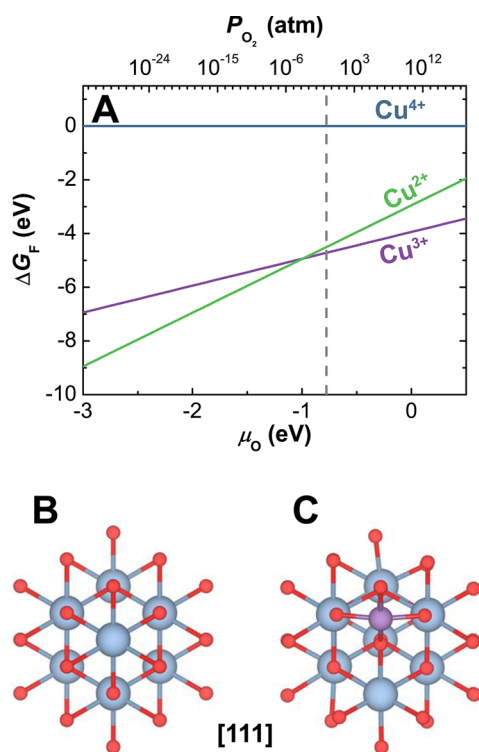


Figure 6. Phase diagram and local molecular structure computed for $\text{Cu}^{(4-x)+}_2\text{Ce}_{34}\text{O}_{72-x}$ models; (A) computed ΔG_F as a function of oxygen chemical potential for three oxidation states of copper in $\text{Cu}^{(4-x)+}_2\text{Ce}_{34}\text{O}_{72-x}$; the local coordination of (B) Ce^{4+} in CeO_2 and of (C) Cu^{3+} in $\text{Cu}^{3+}_2\text{Ce}_{34}\text{O}_{71}$ as viewed down the [111] zone axis. The pressure dependence was calculated at 700 K, with 0.21 atm O_2 indicated by the dashed gray line and the model $\text{Cu}^{4+}_2\text{Ce}_{34}\text{O}_{72}$ was taken as the reference for computing ΔG_F .

transition metal substitution, with XPS predicting an upper bound of as much as 10%. Any disparities in catalytic behavior are due to the electronic structure of the transition metal substitute and not to differences in oxygen-ion vacancy content in these $\text{M}_{0.1}\text{Ce}_{0.9}\text{O}_{2-x}$ compounds.

CO Oxidation Catalysis on CeO_2 and $\text{Cu}_{0.1}\text{Ce}_{0.9}\text{O}_{2-x}$

CO oxidation catalysis was performed on annealed 3 nm $\text{Cu}_{0.1}\text{Ce}_{0.9}\text{O}_{2-x}$ and 3 nm CeO_2 nanoparticles as well as on micrometer-sized CeO_2 to examine if Cu in solid solution with CeO_2 can promote CO oxidation. The experimental “light-off” curves and Arrhenius plots for CO oxidation in oxygen-rich conditions (1% CO, 2.5% O_2) are presented in Figure 7A,B, respectively. Introduction of aliovalent Cu ions into the lattice of CeO_2 lowers the onset temperature for CO oxidation (Figure 7A), and increases the catalytic activity by an order of magnitude compared to CeO_2 nanoparticles and 3 orders of magnitude relative to micrometer-sized CeO_2 (Figure 7B). Preliminary experiments suggest that copper substitution performs at least an order of magnitude better than the other transition metals. Notably, $\text{Cu}_{0.1}\text{Ce}_{0.9}\text{O}_{2-x}$ did not exhibit any irreversible sintering or phase changes during catalysis, even after exposure to 2.5% CO at 300 °C, which suggests that this catalyst could meet the rigorous demand of real-world applications of CO oxidation in catalytic converters or respirators (Figure S24 and Table S9).

The promotion of CO oxidation kinetics with Cu in solid solution with CeO_2 comes as a surprise in light of recent studies which have proposed that the solid solution in CuO-CeO_2

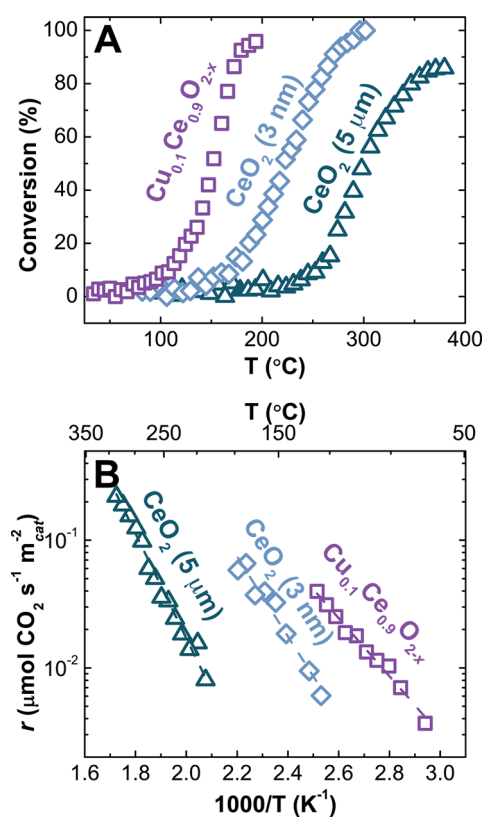


Figure 7. CO oxidation catalysis on annealed 3 nm $\text{Cu}_{0.1}\text{Ce}_{0.9}\text{O}_{2-x}$, 3 nm CeO_2 and commercial 5 μm CeO_2 (Sigma-Aldrich). (A) “Light off” curves and (B) area-normalized Arrhenius plots, measured in 1% CO, 2.5% O_2 balanced in He at a flow rate of 1300 $\text{mL min}^{-1} \text{g}_{\text{cat}}^{-1}$ for 20 mg catalyst loadings.

catalysts is inactive for CO oxidation catalysis, with activities identical to bare, micrometer-sized CeO_2 .^{19,20} Our work calls in to question the origin of the high catalytic activity in mixed phase CuO- CeO_2 catalysts (and mixed-phase ceria-based catalysts in general), which have traditionally been attributed to the interface of crystalline CuO particles with CeO_2 ,^{4,15,19,20,45,46} and therefore offers a new paradigm for the design of CeO_2 -based catalysts.

While the mass-normalized rate of CO oxidation found here for $\text{Cu}_{0.1}\text{Ce}_{0.9}\text{O}_{2-x}$ (0.1 $\mu\text{mol CO s}^{-1} \text{g}_{\text{cat}}^{-1}$ at 35 °C) is significantly smaller than those found under similar conditions for state-of-the-art gold-based catalysts (2.5 and 2.9 $\mu\text{mol CO s}^{-1} \text{g}_{\text{cat}}^{-1}$ for Au/ TiO_2 ⁴⁷ and Au/ CeO_2 ,⁴⁸ respectively), they are comparable to optimized CuO- CeO_2 catalysts (0.12 $\mu\text{mol CO s}^{-1} \text{g}_{\text{cat}}^{-1}$ at 45 °C).⁴⁶ Additionally, the as-synthesized $\text{Cu}_{0.1}\text{Ce}_{0.9}\text{O}_{2-x}$ nanoparticles are extractable in nonpolar organic solvents and hence are particularly suitable for postsynthetic modifications, such as exotemplating,⁴⁹ that would increase the surface area of these materials (and hence their mass-normalized activities) for applications in CO oxidation.

The enhanced activity of CeO_2 nanoparticles relative to micrometer-sized CeO_2 is in agreement with previous work.⁴⁸ The origin of such structure sensitivity has been investigated previously, where it was found that CeO_2 catalysts with exposed {001} and {110} facets give significantly higher rates for CO oxidation than catalysts with predominantly {111} termination.⁵⁰ In the present case, the activity enhancement is likely due to a higher concentration of reactive {001} facets in the

nanostructured CeO₂ (e.g., Figure S13B,CD) compared to micrometer-sized CeO₂, where the low-energy {111} facets are more predominant.⁵¹ This strategy has been exploited, for example, for CO oxidation on gold catalysts where researchers found a two-order of magnitude increase in activity when employing nanostructured CeO₂ over micrometer-sized CeO₂.⁴⁸

The synthetic strategy adopted here thus decouples geometric effects (dispersion, crystallite size) from intrinsic, electronic effects in catalysis, thereby paving a way to develop design descriptors based on the electronic structure of these materials for heterogeneous catalysis. Apparent rates for CO oxidation are functions of the size and shape of the catalyst particles, the dispersion of the active sites on the surface and the intrinsic activity of each active site. The bottom-up synthetic approach outlined here enables the study of the *intrinsic* activity of these solid solutions as a function of their electronic structure and transition metal substitution. The correlation of catalytic activity with the electronic structure of these catalysts will be explored in future studies to search for activity descriptors and potentially establish design guidelines for the development of next-generation CO oxidation catalysts.

CONCLUSIONS

In summary, we have presented a simple and generalizable route for the preparation of monodisperse nanoparticles of transition-metal-substituted ceria (M_{0.1}Ce_{0.9}O_{2-x}, M = Mn, Fe, Co, Ni and Cu). Unlike preparations of similar catalysts by conventional methods, the monodispersity in size and shape, as well as the purity of the resulting single-crystalline M_{0.1}Ce_{0.9}O_{2-x} is well controlled by the solution-based pyrolysis of heterobimetallic Schiff base complexes. To the best of our knowledge, such synthetic control has not previously been demonstrated for such a broad range of transition metal substitutes and has implications not only for the design of novel catalysts but also for the accurate interpretation of catalytic trends and active sites in heterogeneous catalysis. As synthesized, single-crystalline M_{0.1}Ce_{0.9}O_{2-x} materials are soluble in nonpolar organic solvents and, as such, can be further processed into hierarchical assemblies,¹¹ thin films and devices. The bulk and local atomic structure were verified by PXRD, HRTEM and XAS, which suggest that the aliovalent transition metal ions substitute completely into the CeO₂ lattice with truncated octahedral crystalline habits and exposed {100} and {111} facets.

Steady-state CO oxidation catalysis on Cu_{0.1}Ce_{0.9}O_{2-x} reveals that the aliovalent copper ions incorporated into the CeO₂ lattice are responsible for an increase in catalytic activity by an order of magnitude compared to nanocrystalline CeO₂. We also found that nanocrystalline CeO₂ is 2 orders of magnitude more active than bulk CeO₂. These results justify the bottom-up synthetic approach we employ here, where geometrical effects in catalysis are decoupled from purely electronic effects, by comparing surface-area-normalized catalytic rates of substituted CeO₂ of nearly identical size and crystalline habit. These results suggest a new paradigm for the design of CeO₂-based catalysts while simultaneously allowing for systematic correlations between the electronic structure of M_{0.1}Ce_{0.9}O_{2-x} and catalytic activity. Notably and in opposition to previous reports suggesting Cu⁺ or Cu²⁺ to be the active sites for catalysis,^{4,12,16,17,52} XAS studies on the Cu_{0.1}Ce_{0.9}O_{2-x} catalyst reveal that copper exists as an admixture of Cu²⁺ and Cu³⁺ species. These results report, to the best of our knowledge, the

first instance that Cu³⁺ has been implicated in the mechanism for CO oxidation on CuO-CeO₂ catalysts, and, as such, demonstrate that considerable care must be exercised when making claims about the active site for mixed-phase heterogeneous catalysts. The origin of this stabilization of Cu³⁺ and its connection to the high catalytic activity of Cu_{0.1}Ce_{0.9}O_{2-x} warrants further studies, but we hypothesize that the higher activity is due to the accessible Cu³⁺/Cu²⁺ redox couple in Cu_{0.1}Ce_{0.9}O_{2-x}.

ASSOCIATED CONTENT

Supporting Information

The X-ray crystallographic files (CIF) for Co^{III}-Ce^{III}-3-MeO-salpn, Ni^{II}-Ce^{III}-3-MeO-salpn and Cu^{II}-Ce^{III}-3-MeO-salpn, experimental and computational methods, NMR, FTIR, PXRD, HRTEM and XAS characterization. This material is available free of charge via the Internet at <http://pubs.acs.org>.

AUTHOR INFORMATION

Corresponding Authors

E-mail: jselias@mit.edu.

E-mail: shaohorn@mit.edu.

Notes

The authors declare no competing financial interest.

ACKNOWLEDGMENTS

Use of the National Synchrotron Light Source, Brookhaven National Laboratory, was supported by the U.S. Department of Energy, Office of Science, Office of Basic Energy Sciences, under Contract No. DE-AC02-98CH10886. DFT computations in this work were benefited from the use of the National Energy Research Scientific Computing Center allocation of the Center for Nanophase Materials Sciences at Oak Ridge National Laboratory under Grant Number CNMS2013-292. Research described in this paper was also performed at the Canadian Light Source, which is funded by the Canada Foundation for Innovation, the Natural Sciences and Engineering Research Council of Canada, the National Research Council Canada, the Canadian Institutes of Health Research, the Government of Saskatchewan, Western Economic Diversification Canada, and the University of Saskatchewan. This work was partially supported by Philip Morris International. J.S.E. was supported by the National Science Foundation Graduate Research Fellowship under Grant No. DGE-1122374. The X-ray diffractometer used for single-crystal studies was purchased with the help of funding from the National Science Foundation under Grant No. CHE-0946721. The authors would like to thank Ms. Kelsey Stoerzinger at MIT and Ms. Sarah Purdy at University of Saskatchewan for their assistance with soft XAS, Mr. Thomas Carney at MIT for assistance with ICP-AES, and thanks are due to the staff members at beamline X11A at NSLS and beamline SGM at CLS. The authors would like to thank Professor Yuriy Román and his lab at MIT for helpful discussions concerning reactor design and Dr. Peter Müller at MIT for acquiring the single-crystal diffraction data.

REFERENCES

- (1) Martin, D.; Duprez, D. *J. Phys. Chem.* **1996**, *100*, 9429.
- (2) Madier, Y.; Descorme, C.; Le Govic, A. M.; Duprez, D. *J. Phys. Chem. B* **1999**, *103*, 10999.
- (3) Mogensen, M.; Sammes, N. M.; Tompsett, G. A. *Solid State Ionics* **2000**, *129*, 63.
- (4) Liu, W.; Flytzani-Stephanopoulos, M. *J. Catal.* **1995**, *153*, 317.

- (5) Fu, Q.; Saltsburg, H.; Flytzani-Stephanopoulos, M. *Science* **2003**, *301*, 935.
- (6) Chueh, W. C.; Falter, C.; Abbott, M.; Scipio, D.; Furler, P.; Haile, S. M.; Steinfeld, A. *Science* **2010**, *330*, 1797.
- (7) Chueh, W. C.; Hao, Y.; Jung, W.; Haile, S. M. *Nat. Mater.* **2012**, *11*, 155.
- (8) Wang, Z.; Flytzani-Stephanopoulos, M. *Energy Fuels* **2005**, *19*, 2089.
- (9) Liu, Y.; Hayakawa, T.; Suzuki, K.; Hamakawa, S.; Tsunoda, T.; Ishii, T.; Kumagai, M. *Appl. Catal., A* **2002**, *223*, 137.
- (10) Jasinski, P.; Suzuki, T.; Anderson, H. U. *Sens. Actuators, B* **2003**, *95*, 73.
- (11) Corma, A.; Atienzar, P.; Garcia, H.; Chane-Ching, J.-Y. *Nat. Mater.* **2004**, *3*, 394.
- (12) Wang, X.; Rodriguez, J. A.; Hanson, J. C.; Gamarra, D.; Martinez-Arias, A.; Fernandez-Garcia, M. *J. Phys. Chem. B* **2005**, *109*, 19595.
- (13) Dow, W. P.; Huang, T. J. *J. Catal.* **1994**, *147*, 322.
- (14) Wang, X.; Rodriguez, J. A.; Hanson, J. C.; Gamarra, D.; Martinez-Arias, A.; Fernandez-Garcia, M. *J. Phys. Chem. B* **2006**, *110*, 428.
- (15) Gamarra, D.; Munuera, G.; Hungria, A. B.; Fernandez-Garcia, M.; Conesa, J. C.; Midgley, P. A.; Wang, X. Q.; Hanson, J. C.; Rodriguez, J. A.; Martinez-Arias, A. *J. Phys. Chem. C* **2007**, *111*, 11026.
- (16) Soria, J.; Conesa, J. C.; Martinez-Arias, A.; Coronado, J. M. *Solid State Ionics* **1993**, *63 - 65*, 755.
- (17) Martinez-Arias, A.; Fernandez-Garcia, M.; Soria, J.; Conesa, J. C. *J. Catal.* **1999**, *182*, 367.
- (18) Gamarra, D.; Martinez-Arias, A. *J. Catal.* **2009**, *263*, 189.
- (19) Jia, A.-P.; Jiang, S.-Y.; Lu, J.-Q.; Luo, M.-F. *J. Phys. Chem. C* **2010**, *114*, 21605.
- (20) Jia, A.-P.; Hu, G.-S.; Meng, L.; Xie, Y.-L.; Lu, J.-Q.; Luo, M.-F. *J. Catal.* **2012**, *289*, 199.
- (21) Elmali, A.; Elerman, Y. Z. *Naturforsch., B: J. Chem. Sci.* **2003**, *58*, 639.
- (22) Vigato, P. A.; Tamburini, S. *Coord. Chem. Rev.* **2008**, *252*, 1871.
- (23) Akine, S.; Nabeshima, T. *Dalton Trans.* **2009**, 10395.
- (24) Andruh, M. *Chem. Commun.* **2011**, *47*, 3025.
- (25) Deshpande, S.; Patil, S.; Kuchibhatla, S. V. N. T.; Seal, S. *Appl. Phys. Lett.* **2005**, *87*, 133113.
- (26) Turner, S.; Lazar, S.; Freitag, B.; Egoavil, R.; Verbeeck, J.; Put, S.; Strauven, Y.; Van Tendeloo, G. *Nanoscale* **2011**, *3*, 3385.
- (27) Gilliss, S. R.; Bentley, J.; Carter, C. B. *Appl. Surf. Sci.* **2005**, *241*, 61.
- (28) Zhang, F.; Chan, S.-W.; Spanier, J. E.; Apak, E.; Jin, Q.; Robinson, R. D.; Herman, I. P. *Appl. Phys. Lett.* **2002**, *80*, 127.
- (29) Zhang, F.; Jin, Q.; Chan, S.-W. *J. Appl. Phys.* **2004**, *95*, 4319.
- (30) Lin, M.; Fu, Z. Y.; Tan, H. R.; Tan, J. P. Y.; Ng, S. C.; Teo, E. *Cryst. Growth Des.* **2012**, *12*, 3296.
- (31) Nachimuthu, P.; Shih, W.-C.; Liu, R.-S.; Jang, L.-Y.; Chen, J.-M. *J. Solid State Chem.* **2000**, *149*, 408.
- (32) Bianconi, A.; Marcelli, A.; Dexpert, H.; Karnatak, R.; Kotani, A.; Jo, T.; Petiau, J. *Phys. Rev. B: Condens. Matter Mater. Phys.* **1987**, *35*, 806.
- (33) Soldatov, A. V.; Ivanchenko, T. S.; Della Longa, S.; Kotani, A.; Iwamoto, Y.; Bianconi, A. *Phys. Rev. B: Condens. Matter Mater. Phys.* **1994**, *50*, 5074.
- (34) Rehr, J. J.; Albers, R. C. *Rev. Mod. Phys.* **2000**, *72*, 621.
- (35) Flipse, C. F. J.; van der Laan, G.; Johnson, A. L.; Kadowaki, K. *Phys. Rev. B: Condens. Matter Mater. Phys.* **1990**, *42*, 1997.
- (36) Krol, A.; Lin, C. S.; Ming, Z. H.; Sher, C. J.; Kao, Y. H.; Chen, C. T.; Sette, F.; Ma, Y.; Smith, G. C.; Zhu, Y. Z.; Shaw, D. T. *Phys. Rev. B: Condens. Matter Mater. Phys.* **1990**, *42*, 2635.
- (37) Hahn, J. E.; Scott, R. A.; Hodgson, K. O.; Doniach, S.; Desjardins, S. R.; Solomon, E. I. *Chem. Phys. Lett.* **1982**, *88*, 595.
- (38) Brese, N. E.; O'Keeffe, M.; Von Dreele, R. B.; Young, V. G., Jr. *J. Solid State Chem.* **1989**, *83*, 1.
- (39) Grioni, M.; Goedkoop, J. B.; Schoorl, R.; de Groot, F. M. F.; Fuggle, J. C.; Schäfers, F.; Koch, E. E.; Rossi, G.; Esteva, J. M.; Karnatak, R. C. *Phys. Rev. B: Condens. Matter Mater. Phys.* **1989**, *39*, 1541.
- (40) Kaindl, G.; Strelbel, O.; Kolodziejczyk, A.; Schäfer, W.; Kiemel, R.; Lösch, S.; Kemmler-Sack, S.; Hoppe, R.; Müller, H. P.; Kissel, D. *Phys. B (Amsterdam, Neth.)* **1989**, *158*, 446.
- (41) Hu, Z.; Kaindl, G.; Warda, S. A.; Reinen, D.; de Groot, F. M. F.; Müller, B. G. *Chem. Phys.* **1998**, *232*, 63.
- (42) Bianconi, A.; Castellano, A. C.; De Santis, M.; Rudolf, P.; Lagarde, P.; Flank, A. M.; Marcelli, A. *Solid State Commun.* **1987**, *63*, 1009.
- (43) Levason, W.; Spicer, M. D. *Coord. Chem. Rev.* **1987**, *76*, 45.
- (44) Burdett, J. K.; Sevov, S. *J. Am. Chem. Soc.* **1995**, *117*, 12788.
- (45) Liu, W.; Sarofim, A. F.; Flytzani-Stephanopoulos, M. *Chem. Eng. Sci.* **1994**, *49*, 4871.
- (46) Liu, W.; Flytzani-Stephanopoulos, M. *Chem. Eng. J. Biochem. Eng. J.* **1996**, *64*, 283.
- (47) Walther, G.; Mowbray, D. J.; Jiang, T.; Jones, G.; Jensen, S.; Quaade, U. J.; Horch, S. *J. Catal.* **2008**, *260*, 86.
- (48) Carretin, S.; Concepción, P.; Corma, A.; López Nieto, J. M.; Puentes, V. F. *Angew. Chem., Int. Ed.* **2004**, *43*, 2538.
- (49) Schuth, F. *Angew. Chem., Int. Ed.* **2003**, *42*, 3604.
- (50) Zhou, K.; Wang, X.; Sun, X.; Peng, Q.; Li, Y. *J. Catal.* **2005**, *229*, 206.
- (51) Wang, Z. L.; Feng, X. *J. Phys. Chem. B* **2003**, *107*, 13563.
- (52) Sedmak, G.; Hocevar, S.; Levec, J. *J. Catal.* **2004**, *222*, 87.